Journal Pre-proof

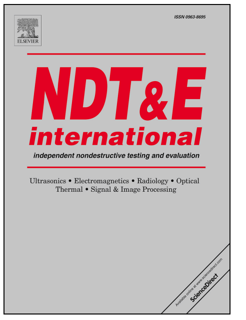

Nonlinear Local Wave-Direction Estimation for In-sight and Out-of-sight Damage Localization in Composite Plates

Joost Segers, Saeid Hedayatrasa, Gaétan Poelman, Wim Van Paepegem, Mathias Kersemans

PII: S0963-8695(21)00011-6

DOI: https://doi.org/10.1016/j.ndteint.2021.102412

Reference: JNDT 102412

To appear in: *NDT and E International*

Received Date: 7 August 2020

Revised Date: 29 October 2020

Accepted Date: 14 January 2021

Please cite this article as: Segers J, Hedayatrasa S, Poelman G, Van Paepegem W, Kersemans M, Nonlinear Local Wave-Direction Estimation for In-sight and Out-of-sight Damage Localization in Composite Plates, *NDT and E International*, https://doi.org/10.1016/j.ndteint.2021.102412.

CRediT author statement

Joost Segers: Conceptualization, Methodology, Software, Writing—original draft preparation

Saeid Hedayatrasa: Conceptualization, Validation, Writing—review and editing

Gaétan Poelman: Validation, Writing—review and editing

Wim Van Paepegem: Resources, Writing—review and editing, Supervision, Funding acquisition

Mathias Kersemans: Conceptualization, Resources, Writing—review and editing, Supervision, Funding acquisition

All authors have read and agreed to the published version of the manuscript.

Nonlinear Local Wave-Direction Estimation for In-sight and Out-of-sight Damage Localization in Composite Plates

Joost Segers[1#], Saeid Hedayatrasa[1,2], Gaétan Poelman[1], Wim Van Paepegem[1] and Mathias Kersemans[1#]

[1] Mechanics of Materials and Structures (UGent-MMS), Department of Materials, Textiles and Chemical Engineering (MaTCh), Ghent University, Technologiepark-Zwijnaarde 46, 9052 Zwijnaarde, Belgium

[#] Corresponding authors: Joost.Segers@ugent.be, Mathias.Kersemans@ugent.be

[2] SIM Program M3 DETECT-IV, Technologiepark-Zwijnaarde 48, B-9052 Zwijnaarde, Belgium

Abstract

In this study, a novel wave processing algorithm: "local wave-direction estimation (LWDE)", is proposed to localize sources of guided waves using full-field scanning laser Doppler (SLDV) measurements. The LWDE algorithm uses angular bandpass filters in the wavenumber domain to determine the local propagation direction of the guided wave. The obtained local wave-direction map is converted into an error map by the use of a virtual local wave-direction map. The resulting error map reveals the sources of guided waves as local minima. The exploitation of local directional wave information provides the opportunity to scan only a small part of the component for localization of out-of-sight sources of guided waves. The source localization performance of LWDE is illustrated for localization of multiple piezoelectric sources in a quasi-isotropic CFRP plate.

LWDE is further coupled to nonlinear vibrations in view of damage localization (NL-LWDE). The second higher harmonic component is extracted from the SLDV measurement and the sources of this higher harmonic component are localized. Damages behave as sources of higher harmonics and are thus localized by this NL-LWDE approach. This is demonstrated for a cross-ply CFRP plate with low velocity impact damage. The proposed combination of (i) nonlinear vibration filtering, (ii) direction estimation using angular bandpass filtering in the wavenumber domain and (iii) error map construction using the virtual wave-direction map results in a robust and baseline-free NDT technique. It can be used for accurate localization of multiple in-sight or out-of-sight damages in composite plates with unknown material properties and layup.

Keywords

Composites; Non-destructive testing (NDT); Ultrasonic guided waves; Local wave-direction estimation (LWDE); Nonlinearity; Higher harmonics; Scanning laser Doppler vibrometry

1. Introduction

Layered fiber reinforced polymer materials or composites are nowadays used in state-of-the-art components where they replace traditionally used metal alloys. The use of composites, especially carbon fiber reinforced polymers (CFRP), is beneficial for weight saving purposes thanks to their design flexibility and high specific strength and stiffness. As a result, CFRPs are extensively used in the aerospace industry. A critical hurdle in the use of layered composite components is their susceptibility to internal defects or damage. These defects can be introduced during the manufacturing process or during the operational lifetime of the component. A well-known type of internal damage is barely visible impact damage (BVID), which consists of multiple delaminations and cracks and is formed by low velocity impacts (e.g. tool drop or bird strike). Internal defects decrease the global strength and stiffness of the component which can eventually lead to unexpected failure. In order to guarantee the safe operation using composite components, non-destructive testing (NDT) is performed both after manufacturing and at regular intervals during the operational life.

A large variety of NDT methods exist of which the immersion ultrasonic C-scan is often used to find defects in composite structures made for aerospace applications [1]. The immersion ultrasonic C-scan allows accurate detection and evaluation of damages plate-like structures. On the other hand, it is relatively slow (i.e. point wise excitation and measurement) and the needed coupling medium, or immersion, imposes practical difficulties. As an alternative, the analysis of guided waves or Lamb waves measured at the surface of thin-walled composites can be used for damage detection. Guided waves travel throughout large inspection areas with relatively low loss and interact with various defect types through the thickness. The guided waves of interest for performing NDT are typically in the 10 to 300 kHz range and are excited using either piezoelectric actuators [2], air coupled ultrasonic actuators [3] or high power excitation lasers [4]. The full wavefield response is most often recorded remotely using a scanning laser Doppler vibrometer (SLDV). Doing so, a three-dimensional dataset is obtained of the full wavefield response in function of time. The propagating nature of a guided wave allows to detect defects (and actuators) which may be hidden behind other structures, as will be shown later in the manuscript.

The local characteristics of the guided waves, e.g. frequency, wavenumber, amplitude and mode type, depend on the local characteristics of the material, i.e. (visco-)elastic stiffness tensor and material thickness. A defect causes a local change in these material characteristics which in turn alters the characteristics of the observed guided waves. In the last decades, multiple NDT approaches were developed in order to construct damage maps by searching for these anomalies in the guided wave characteristics [2].
A first class of full wavefield NDT methods are those which exploit linear wave-defect interactions. Within this class, there are the methods which use the local change in wavenumber of a guided wave at a defect. These methods are referred to as local wavenumber estimation, acoustic wavenumber spectroscopy or instantaneous wavenumber estimation [4-8], depending on the implementation of the method. Other linear guided wave NDT methods focus on the local change in wave amplitude or energy rather than the change in wavenumber. When a wave packet interacts with a delamination defect, the wave energy becomes partially trapped at the defect. This phenomenon is commonly referred to as ‘mode trapping’ or ‘wave energy trapping’ and is also related to local defect resonance [9-17]. The trapping of the wave energy results in a local increase in vibrational amplitude. These high energy spots can be detected using weighted-root-mean-square energy mapping [11]. In addition, a combination of the energy and the wavenumber methods has also been applied, where wavenumber filtering is performed prior to weighted-root-mean-square energy calculation [18, 19]. While these NDT methods show promising results, they lack the sensitivity to detect very small and very deep defects [8, 16, 20]. Improved sensitivity to small and deep defects is obtained when using a broadband wavenumber filtering and energy mapping approach [21].

There also exists a second class of full wavefield NDT methods which operate in the nonlinear regime. They exploit the non-classical nonlinear response of a defect caused by contact acoustic nonlinearity, hysteresis and friction [22, 23]. As a result of contact acoustic nonlinearity, new vibrational components are formed at the defect with a frequency different to the frequency of the incoming vibrations. These methods were developed in order to further increase the sensitivity to small and deep defects. One speaks about nonlinear elastic wave spectroscopy (NEWS) [24-30] or nonlinear elastic wave modulation spectroscopy (NEWMS) [31-36], when there is a single excitation or when there are multiple excitation signals, respectively. Very recently, the current authors used (numerical as well as experimental) NEWS to show that the nonlinear response at the defect can be used for the detection of shallow damages and, more important, deep backside delaminations [37, 38]. It was observed that defects act as secondary sources of higher harmonic vibrational components which can be measured at a distance from the defect's location.

In this manuscript, we build further on the observation that both shallow and deep defects act as sources of nonlinear vibrational components. A novel source localization algorithm, named "(Nonlinear) Local wave-direction estimation (NL-LWDE)", is proposed to localize the defect as a source of nonlinear vibrations. Over the entire scan area, the local direction of the propagating waves is determined using angular bandpass filters in the wavenumber domain. The observed local wave-direction map is then converted into an error map where the sources (i.e. actuators and damages) are identified as local minima. The proposed NL-LWDE method proves successful for the detection of (out-of-sight) BVID.

The manuscript is split up into two major parts. In the first part, the process of source localization using the local wave-direction estimation LWDE algorithm is outlined and all processing steps are discussed in detail. For this, the measurement results of a damage-free quasi-isotropic CFRP plate are used. The plate is excited with piezoelectric actuators and the LWDE is used to find the location of the in-sight and out-of-sight sources. In the second part, the LWDE algorithm is used in the nonlinear regime (i.e. NL-LWDE) for the detection of BVID in a cross-ply CFRP plate. It is illustrated that the damage can be detected and localized in a baseline-free and automated manner. Moreover, it is shown that the proposed NDT method can equally be used in case that the defects are located outside of the measured wavefield (i.e. out-of-sight damage).

2. Material and Measurement

Two CFRP test specimens are used in this manuscript (see Figure 1).

Both plates measure 330x330x5.54 mm^3 and are manufactured out of 24 layers of unidirectional carbon fiber prepreg. The first plate (Figure 1(a)) is manufactured using a quasi-isotropic $[(+45/0/-45/90)_3]_s$ lay-up. No defects or damages are present. The second plate (Figure 1(b)) is manufactured using a cross-ply layup $[(0/90)_6]_s$ and has been impacted with a 7.7 kg drop weight from a height of 0.09 m (i.e. impact energy 6.8 J) according to ASTM D7136. The low velocity impact resulted in BVID. To reveal the extent of the damage, an immersion ultrasonic C-scan inspection is performed using a 5 MHz focused transducer (H5M, General Electric) in reflection mode. The C-scan relative amplitude image reveals the complex distribution of delaminations and cracks, which is typical for low velocity impact damage in layered composite materials [39]. The plate is inspected from the impact side.

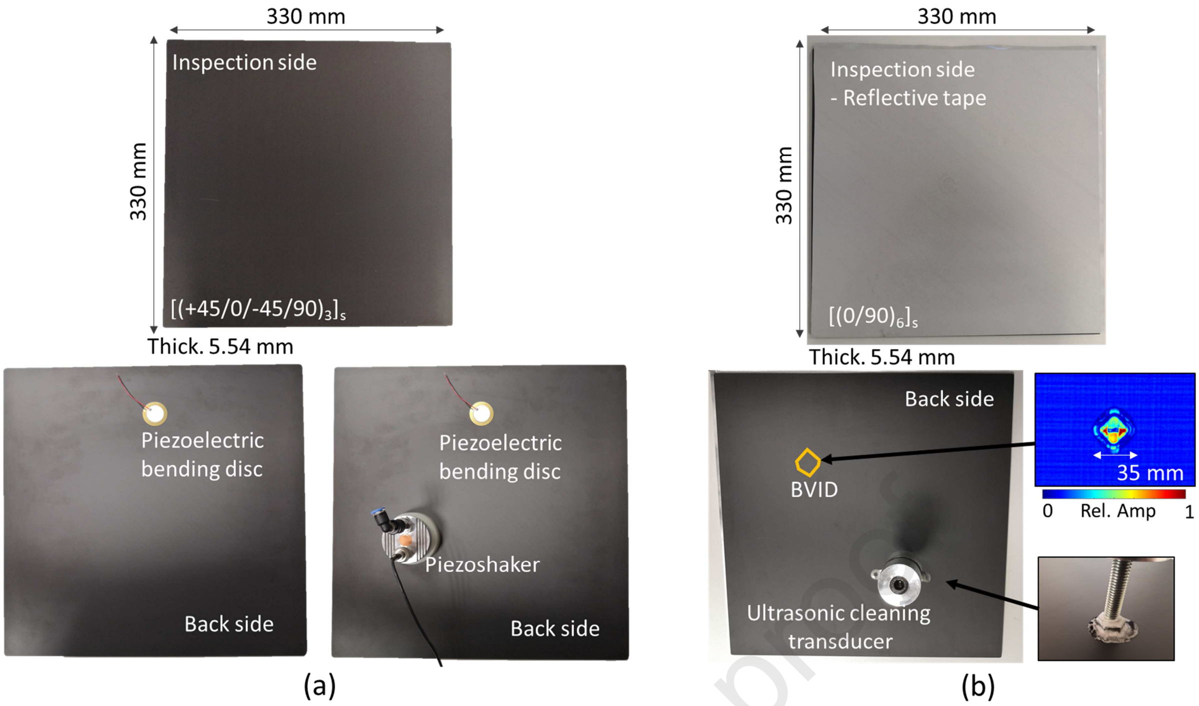

Figure 1: CFRP components: (a) Damage-free quasi-isotropic plate, (b) Cross-ply plate with BVID.

Vibrations are introduced using piezoelectric actuators. For the damage-free CFRP plate (see Figure 1(a)), two different actuators are used: a small piezoelectric bending disc (Ekulit EPZ-20MS64W) and a larger piezoshaker (isi-sys PS-X-03-6/1000). The bending disc is bonded to the plate using phenyl salicylate while the piezoshaker is attached by vacuum. The use of vacuum and phenyl salicylate allows to easily remove the actuators after the measurements without damaging the component's surface. A 5-cycle Hanning-windowed toneburst signal with center frequency 100 kHz is used for exciting the propagating waves. Two separate measurements are performed. First, only the bending disc actuator is attached and used for excitation. Next, the piezo shaker is added and both actuators are supplied with the same excitation signal. This allows to explain the LWDE algorithm first for the simple case of a single source and afterwards for the case of multiple sources (see Section 3.1 and 3.2 respectively). A Falco WMA-300 voltage amplifier is used to increase the excitation signal to a peak-to-peak voltage of 250 V.

For the CFRP plate with BVID damage (see Figure 1(b)), an ultrasonic cleaning transducer (with nominal cleaning power 70 W and resonance frequency 120 kHz) is used as it can deliver more vibrational power. A M10 bolt is screwed into the transducer and serves as a stinger, leading to a relative small contact area between the source and the plate. Again, phenyl salicylate is used to temporarily bond the actuator to the plate (see inset on Figure 1(b)). The actuator is supplied with a linear sweep voltage signal from 10 kHz to 125 kHz with amplified peak-to-peak voltage of 350 V.

Table 1 summarizes the characteristics of the excitation signals.

The full wavefield velocity response of the components is measured using a 3D SLDV with infrared measurement lasers (Polytec PSV-500-3D Xtra). The measurement settings are listed in Table 1. The infrared lasers show high sensitivity, even on black surfaces. However, as the excitation power is relatively low, averages are taken to increase the signal-to-noise ratio of the measurements. In addition, the plate with BVID is covered with removable reflective tape (3M™ Scotchlite™ 680CRE10). This was required to be able to detect the nonlinear vibrational components which are of low amplitude [23, 37, 38]. In both cases, the propagation of the fundamental anti-symmetric Lamb mode (A_0), which has a dominant out-of-plane surface velocity response, is investigated. As a result, only the out-of-plane velocity component (V_Z) is considered.

Table 1: Excitation and measurement settings.

Sample	Excitation signal						SLDV			
	Type	f_{start} (kHz)	f_c (kHz)	f_{end} (kHz)	Voltage (Vpp)	Duration (ms)	Sample freq (kHz)	Samples #	Averages #	Scan grid (mm)
Virgin	Toneburst		100		250	0.8	1250	1000	10	2.5
BVID	Lin. sweep	10		125	350	40	625	25000	3	2.5

3. Source localization using local wave-direction estimation

The local wave-direction estimation (LWDE) method is introduced for the measurement results of a damage-free quasi-isotropic CFRP plate with multiple sources of propagating waves. First, the LWDE is used for the detection of a single in-sight source of A_0 mode waves (i.e. the piezoelectric bending disc). Next, the algorithm is extended to detect multiple sources. At last, it is shown that LWDE can equally be used for the detection of multiple out-of-sight sources.

The different steps of the algorithm are schematically illustrated in Figure 2. The procedure is inspired by the local wavenumber estimation algorithm proposed by Flynn et al. [4] and combines extensive filtering in the wavenumber-frequency domain as proposed by Michaels et al. [40].

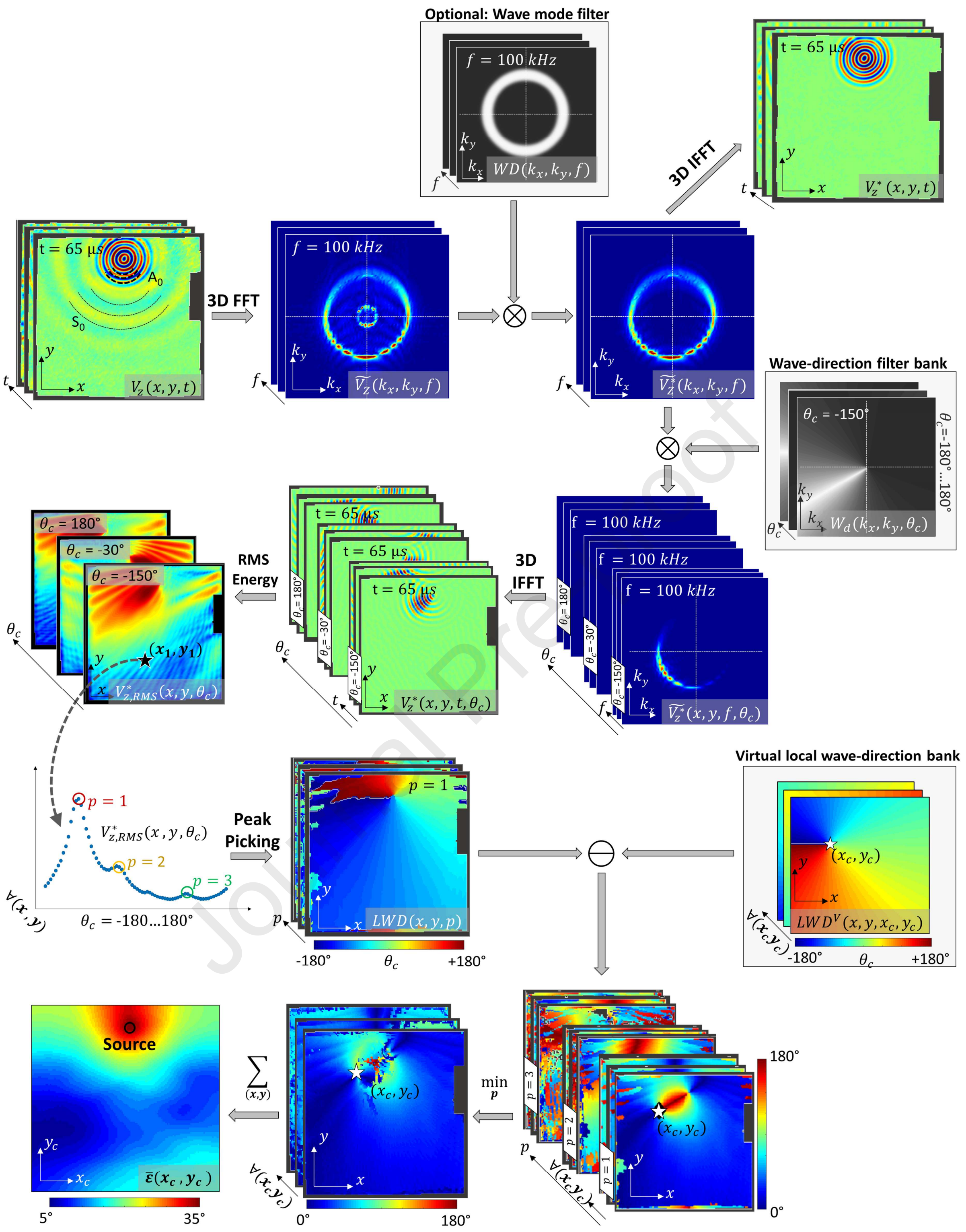

Figure 2: Source localization using local wave-direction estimation.

3.1. LWDE – Single source, in-sight

As a first experiment, only the piezoelectric bending disc is used to excite the plate with propagating waves. An animation of this burst response is made available as supplementary material. Figure 3(a) shows a snapshot in time at t = 0.065 ms. From this figure (and the animation) it is seen that there are two propagating Lamb modes: A_0 and S_0.

a. Data conditioning – A_0 mode bandpass filtering

In order to improve the source localization using LWDE, the burst response is first filtered and only the A_0 mode wave vibrations are retained. The mode bandpass filter is applied in the wavenumber-frequency (k_x, k_y, f) domain [40]. First, the burst response $V_z(x, y, t)$ is transformed to the (k_x, k_y, f) domain using the 3D Fourier transform:

$$\tilde{V}_z(\mathrm{k_x}, \mathrm{k_y}, \mathrm{f}) = \frac{1}{N.N_x.N_y} \sum_{p=0}^{N_x-1} \left(\sum_{q=0}^{N_y-1} \left(\sum_{n=0}^{N-1} V_z(\mathrm{x}, \mathrm{y}, \mathrm{t}) e^{-2\pi i \frac{k\,n}{N}} \right) e^{-2\pi i \frac{s\,q}{N_y}} \right) e^{-2\pi i \frac{r\,p}{N_x}} \tag{1}$$

With discrete variables: horizontal coordinate $x = [x_1 \dots x_{Nx}]$, vertical coordinate $y = [y_1 \dots y_{Ny}]$, time instance $t = [t_1 \dots t_N]$, horizontal wavenumber $k_x = [k_{x_1} \dots k_{x_{Nx}}]$, vertical wavenumber $k_y = [k_{y_1} \dots k_{y_{Ny}}]$, frequency $f = [f_1 \dots f_N]$ and corresponding indices: $r = [-\frac{N_x-1}{2}, \dots, \frac{N_x-1}{2}]$, $s = [-\frac{N_y-1}{2}, \dots, \frac{N_y-1}{2}]$ and $k = [-\frac{N-1}{2}, \dots, \frac{N-1}{2}]$, respectivley. The $\sim$ symbol indicates the representation in frequency domain.

The wavenumber-frequency map for k_y = 0 is shown in Figure 3(b) and reveals the dispersion curves of both the A_0 and S_0 mode. In order to extract only the vibrations corresponding to the A_0 mode, a cosine-shaped (to avoid leakage in the wavenumber domain) bandpass filter WD is constructed:

$$WD(\mathrm{k_x}, \mathrm{k_y}, \mathrm{f}) = \begin{cases} \frac{1}{2} + \frac{1}{2} cos\left(\frac{2\,\pi\, d(\mathrm{k_r}, \mathrm{f})}{BW}\right) & if\ d(\mathrm{k_r}, \mathrm{f}) < \frac{BW}{2} \\ 0 & elsewhere \end{cases} \tag{2}$$

$$\text{with} \quad k_r = \sqrt{k_x^2 + k_y^2}, \quad d(\mathrm{k_r}, \mathrm{f}) = |k_r - k^{A_0}(f)|$$

with $k^{A_0}(f)$ the dispersion curve of the A_0 mode and bandwidth BW = 75 1/m. The filter WD is multiplied with the burst response $\tilde{V}_z$ in the wavenumber-frequency domain:

$$\tilde{V}_z^{A0}(k_x, k_y, f) = WD(\mathrm{k_x}, \mathrm{k_y}, \mathrm{f}).\tilde{V}_z(k_x, k_y, f) \tag{3}$$

The resulting wavenumber-frequency map (again for k_y = 0) is shown in Figure 3(c). At last, the inverse 3D Fourier transformation is performed to obtain the desired A_0 toneburst response in spatial-time domain:

$$V_z^{A0}(\mathrm{x}, \mathrm{y}, \mathrm{t}) = \sum_{n=0}^{N-1} \left(\sum_{q=0}^{N_y-1} \left(\sum_{p=0}^{N_x-1} \tilde{V}_Z^{A0}(k_x, k_y, f) e^{2\pi i \frac{k\,n}{N_x}} \right) e^{2\pi i \frac{s\,q}{N_y}} \right) e^{2\pi i \frac{r\,p}{N}} \tag{4}$$

Figure 3(d) shows the snapshot in time of the filtered signal where it is seen that the S_0 mode is successfully removed. In addition, this A_0 mode bandpass filtering results in a reduction of the measurement noise. An animation of the V_z^{A0} burst response is provided as supplementary material. Note that the snapshots, as well as the A_0 mode bandpass filter in the wavenumber domain (at 100 kHz), are also shown in the schematic overview of Figure 2.

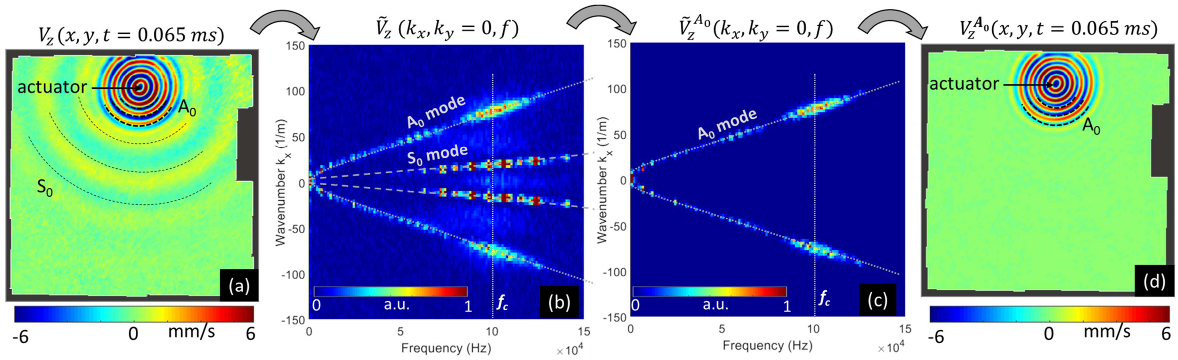

Figure 3: Mode bandpass filtering of A_0 mode in burst response: (a,d) Snapshot at 0.065 ms for the total and the A_0 mode bandpass filtered response, respectively (b,c) Wavenumber-frequency map (at k_y = 0) for the total response and the A_0 mode bandpass filtered response, respectively.

b. LWDE - Wave-direction filter bank

The response signal $\tilde{V}_z^{A0}(k_x, k_y, f)$ is shown in Figure 4(a) at f = 100 kHz, in which the A_0 mode is visible as a circle of increased intensity. Next, the signal is ran through a bank of Gaussian-shaped wave-direction bandpass filters W_d which are defined as:

$$W_d(k_x, k_y, \theta_c) = exp\left(\frac{\angle(k_x, k_y) - \theta_c}{0.72\ BW_\theta}\right) \tag{5}$$

where $\angle(k_x, k_y)$ denotes the angle of the $[k_x, k_y]$ vector, BW_θ is the filter's angular width and $\theta_c = [-180 \ldots -5, 0, 5 \ldots 180]$ is the bandpass center angle. As an example, the bandpass filter for θ_c = -30° and BW_θ = 7° is shown in Figure 4(b). The response after applying this filter: $\tilde{V}_z^{A_0}(k_x, k_y, f, \theta_c) = W_d(k_x, k_y, \theta_c).\tilde{V}_z^{A_0}(k_x, k_y, f)$, is shown in Figure 4(c). This specific bandpass filter results in the extraction of all the vibrations for which the propagation direction $\angle(k_x, k_y)$ is close to θ_c = -30°, i.e. waves travelling in the downward-right direction [40]. Inverse 3D Fourier transformation takes the signal back to the spatial-time domain. Figure 4(d) shows the snapshot in time of the total response at 0.14 ms and Figure 4(e,f) show the corresponding snapshots of the filtered responses with center angle θ_c = -30° and θ_c = -110°, respectively. Note again, that the different processing steps discussed here are also included in Figure 2 as an aid in understanding the algorithm.

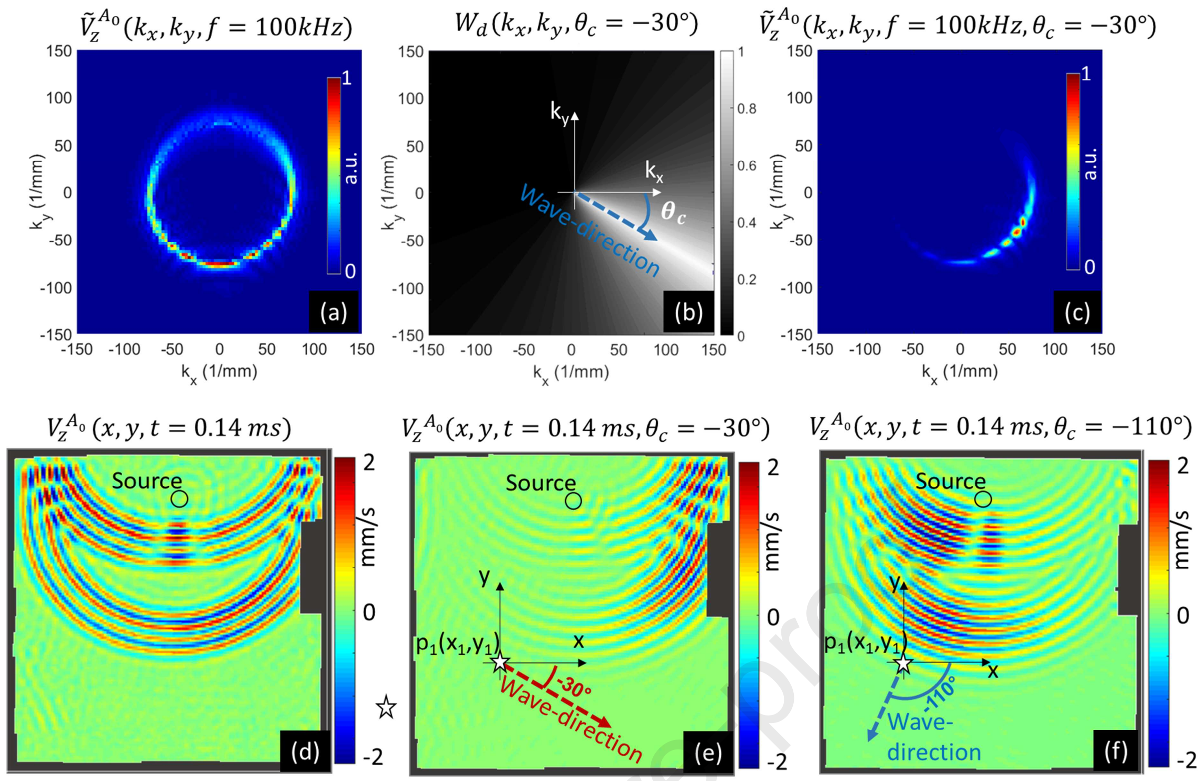

Figure 4: Illustration of the wave-direction bandpass filtering procedure for the A_0 burst response. (a) Wavenumber map at f = 100 kHz. (b) Bandpass filter with θ_c = -30° (c) Bandpass filtered wavenumber map (d) Snapshot of burst response at 0.14 ms (e,f) Snapshot of bandpass filtered burst response at 0.14 ms with θ_c = -30° and θ_c = -110°, respectively.

c. LWDE - Direction detection

After the wave-direction bandpass filter, a 4D dataset $V_z^{A_0}(x, y, t, \theta_c)$ is obtained where the last dimension corresponds to the propagation direction of the guided waves. As an example, the $V_z^{A_0}(x, y, t, \theta_c)$ signal is shown in Figure 5(a) for the scan point $p_1(x_1, y_1)$ and two propagation directions θ_c = -30° and -110°. The location of this point is indicated with a star on Figure 4(e,f). From Figure 5(a) it is observed that the vibrations along direction θ_c = -110° have more energy compared to the vibrations along θ_c = -30°. In order to find the dominant propagation direction at each scan point, the energy of the waves travelling in each θ_c direction is determined as the root-mean-square (RMS) of $V_z^{A_0}(x, y, t, \theta_c)$ over time:

$$V_{z,\,RMS}^{A_0}(x, y, \theta_c) = \frac{1}{N}\sqrt{\sum_{i=1}^{N}\left(V_z^{A_0}(x, y, t_i, \theta_c)\right)^2} \qquad (6)$$

Figure 5(b) shows the obtained energy curve $V_{z,\,RMS}^{A_0}(x_1, y_1, \theta_c)$ for the point $p_1(x_1, y_1)$. Peak picking algorithm is used to automatically determine the local maxima in the curve (indicated on Figure 2 with *Peak picking*). For point $p_1(x_1, y_1)$, a dominant propagation direction is found at θ_c = -110°. This direction is indicated with a blue arrow on Figure 5(c) and correctly points towards the source of vibrations. Other local maxima of lower intensity are visible in the energy curve at around -30°, +100° and 22°. These small maxima correspond to edge reflections of the excited wave packet. This is illustrated on Figure 5(c) for the wave with propagation direction -30°.

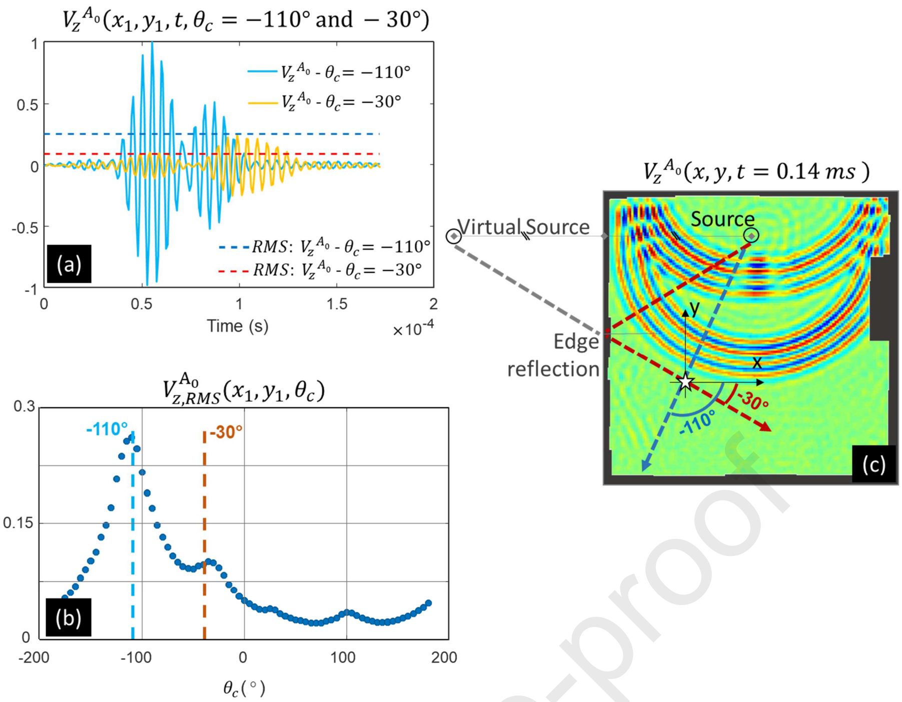

Figure 5: (a) Velocity signal corresponding to the A_0 mode at scan point $p_1(x_1, y_1)$ for waves travelling in the 30° and -110° directions. (b) RMS energy of A_0 mode travelling wave in function of the propagation direction. (c) Snapshot of burst response at 0.14 ms with indication of wave propagation directions.

This direction detection procedure is repeated for every scan point, resulting in the local wave-direction map $LWD(x, y)$. The $LWD(x, y)$ map is shown in Figure 6(a). From this figure, the location of the actuator is clear as for the majority of the scan points a dominant wave propagation direction is found which points to the source's location. Note that the flowchart shown in Figure 2 shows a stack of LWD maps corresponding to the order *p* of the detected peaks in the $V_{z,\,RMS}^{A_0}(x_1, y_1, \theta_c)$ curve. For the detection of a single source, only the first LWD map is required corresponding to *p = 1*. In case of multiple sources, or when dealing with strong edge reflections, all LWD maps must be taken into account as will be explained in Section 3.2.

d. LWDE - error map

While the location of the source could already be distinguished in the $LWD(x, y)$ map, this might not be the case anymore for more challenging test cases (see further). Therefore, it is proposed to use a virtual local wave-direction map $LWD^V(x, y, x_c, y_c)$ for the construction of an error map. The virtual local wave-direction map LWD^V is constructed by assuming that the point with coordinates (x_c, y_c) is the only source of propagating waves:

$$LWD^V(x, y, x_c, y_c) = \angle(x - x_c, y - y_c) \qquad (7)$$

As an example, the LWD^V is plotted in Figure 6(b) for the scan point $p_1(x_1, y_1)$ indicated with the white star. Important to note is that this definition of the LWD^V map assumes a circular wave energy flow. This assumption is valid for (quasi-)isotropic materials. In case of anisotropic materials, it is important to use the A_0 mode (see also Section 3.1.a) as this mode is less affected by the anisotropy compared to for instance the S_0 mode.

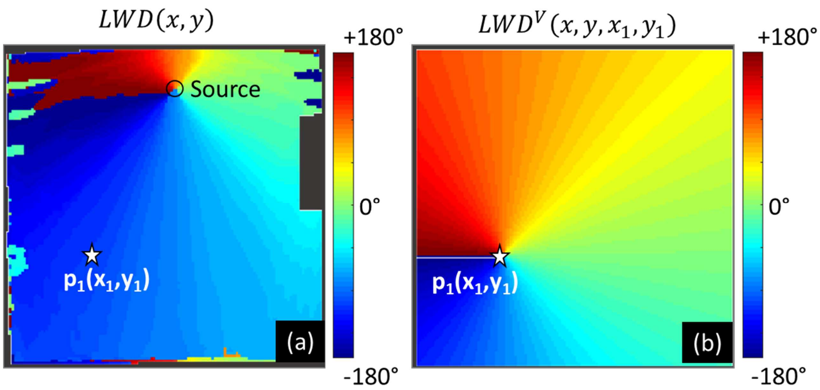

Figure 6: Damage-free CFRP plate with 1 source (a) Observed local wave-direction map (b) Virtual local wave-direction map in case point $p_1(x_1,y_1)$ is a source.

Next, for each point (x_c,y_c) the difference (in degrees) between the observed LWD map and the virtual LWD^V map is calculated (see also Figure 2). The error $\bar{\epsilon}$ is then obtained as the average of this difference over all points:

$$\bar{\epsilon}(x_c,y_c) = \frac{1}{N_x\,N_y}\sum_{(x,y)}|LWD(x,y) - LWD^V(x,y,x_c,y_c)| \tag{8}$$

The resulting error map $\bar{\epsilon}(x_c,y_c)$ is shown in Figure 7. A low error value at a point indicates that the virtual LWD^Vmap for this point is similar to the observed LWD map. As such, the source is found as a local minimum in the obtained error map $\bar{\epsilon}(x_c,y_c)$ (note the inverted colorbar).

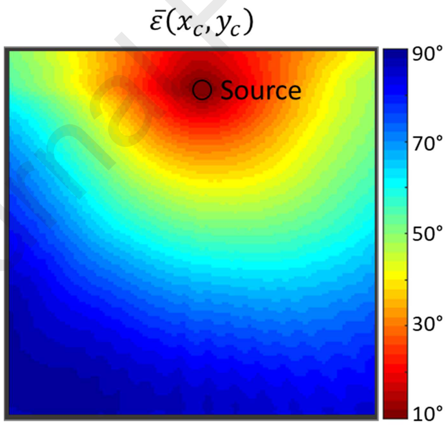

Figure 7: Damage-free CFRP plate with 1 source: Local wave-direction error map.

3.2. LWDE – Multiple sources, in-sight

In the previous section, there was only a single source of propagating waves. Now, the experiment is repeated using two actuators (see Figure 1(a)). Figure 8(a) shows a snapshot in time of the A_0 mode filtered burst response $V_z^{A_0}(x,y,t)$ at t = 0.1 ms. The explanatory point $p_2(x_2,y_2)$ is marked with a white star. A complete animation of the burst response is made available as supplementary material.

All processing steps are identical to the previous case up to the direction detection (see Figure 2 – *Find Peaks* θ_c). For the marked point $p_2(x_2,y_2)$, the RMS energy in function of the propagation direction is shown in Figure 8(b). In this case, two local maxima (or peaks) are found at θ_c = -70° and θ_c = 15°. These directions correspond to the direction of the piezoelectric bending disc (Source 1) and piezoshaker (Source 2), respectively (see arrows on Figure 8(a)). All detected peaks in the RMS curve are sorted according to their maximum value and denoted with integer *p*. As such, the global maximum (i.e. the highest peak) corresponds to *p* = 1. This multi-direction detection is performed for each scan point leading to a three dimensional observed local wave-direction dataset: $LWD(x, y, p)$.

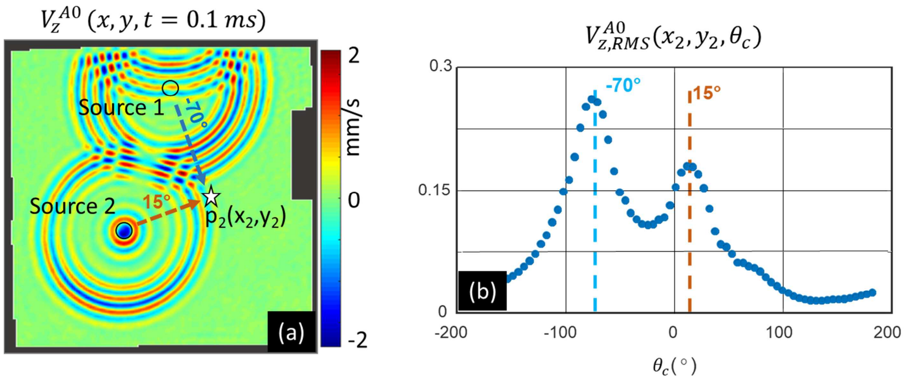

Figure 8: Damage-free CFRP plate with 2 sources: (a) Snapshot at 0.1 ms (b) RMS energy curve for the point $p_2(x_2, y_2)$.

As an example, the $LWD(x, y, p = 1)$ and $LWD(x, y, p = 2)$ maps are shown in Figure 9(a) and (b), respectively. The detected θ_c angles are indicated for the explanatory point $p_2(x_2, y_2)$. Point $p_2(x_2, y_2)$ is located at nearly equal distances from both sources. However, Source 1 (i.e. the bending disc) has a higher vibrational power output. As a result, the primary (*p* = 1) wave propagation direction at point $p_2(x_2, y_2)$ corresponds to Source 1 (see Figure 9(a)) while the secondary (*p* = 2) wave propagation direction at point $p_2(x_2, y_2)$ corresponds to Source 2 (see Figure 9(b)).

The edges of the component are not damped leading to the edge reflection of the propagating waves (see also previously in Figure 5(c)). The resulting edge reflections are visible in the $LWD(x, y, p = 2)$ map (see Figure 9(b)). For instance, above Source 1 a local wave direction is found corresponding to downward travelling waves (i.e. $\theta_c < 0°$). This directions corresponds to the waves excited by Source 1 which are reflected by the top edge of the component.

The equation for the calculation of the error map (Eq. 8) is adapted to allow for multiple source identification and to deal with the presence of the edge reflections (see also Figure 2):

$$\bar{\epsilon}(x_c, y_c) = \frac{1}{N_x\, N_y} \sum_{(x,y)} \min_p |LWD(x, y, p) - LWD^V(x, y, x_c, y_c)| \tag{9}$$

The resulting global error map $\bar{\epsilon}(x_c, y_c)$ is shown in Figure 9(c). The two sources are correctly found as local minima in this error map. The observed edge reflections in Figure 9(b) correspond to virtual sources which are located outside of the structure (see also previously in Figure 5(c)). As a result, they have only a minor effect on the obtained error map and don't increase the error value at the actual sources. Also for the case of a single source, the error map $\bar{\epsilon}(x_c, y_c)$ is improved when using Eq. 9 instead of Eq. 8. This is seen by comparing the error map $\bar{\epsilon}(x_c, y_c)$ calculated using Eq. 9 (see last step in Figure 2) with the error map $\bar{\epsilon}(x_c, y_c)$ calculated using Eq. 8 (see Figure 7).

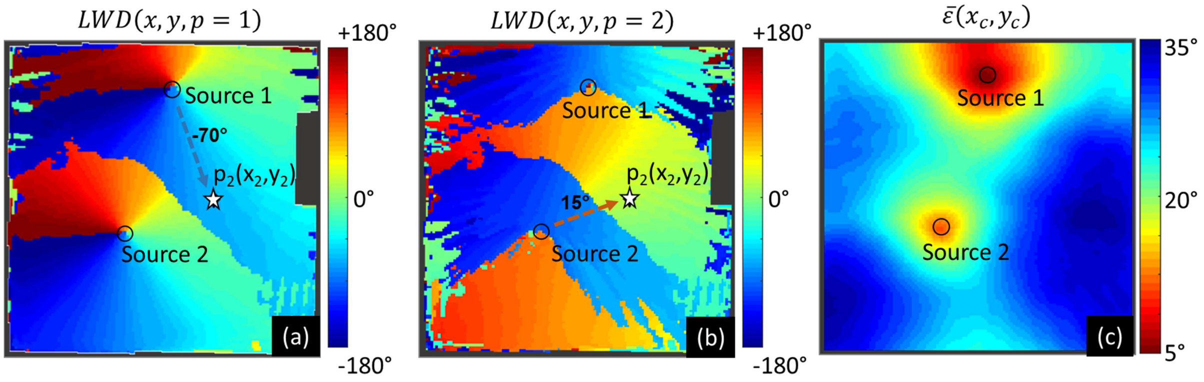

Figure 9: Damage-free CFRP plate with 2 sources: Local wave-direction maps for (a) *p* = 1 and (b) *p* = 2 (c) Local wave-direction error map.

3.3. LWDE – Multiple sources, out-of-sight

As a last step, it is illustrated that the LWDE algorithm equally works for the detection of sources which are not part of the measurement area (i.e. out-of-sight). This allows to find sources (and damages) which are hidden behind other structures. It could also be exploited to reduce the measurement time as the SLDV would only need to scan part of the component.

Here, the out-of-sight source localization is illustrated for two cases where the incomplete scan areas are indicated with green rectangles on Figure 10(a) and (b). All processing steps are identical to Section 3.2 with the exception that only part of the measurement dataset is utilized. In order to increase the resolution in the wavenumber domain, the incomplete scan area is zero-padded in spatial domain so that the amount of points is identical to the case where the total area was scanned.

First, the local wave-direction maps $LWD(x, y, p)$ are determined. The obtained $LWD(x, y, p = 1)$ maps are superimposed on Figure 10(a,b). Next, the damage maps are constructed using Eq. 9. The coordinates (x_c, y_c) span the entire component, whereas the points (x, y) are limited to the incomplete scan area. The resulting error maps $\bar{\varepsilon}(x_c, y_c)$ are shown in Figure 10(c,d). For each of these maps, a reduced error value is found at the location of the sources.
The use of only a small part of the component's surface response leads to a correct but less accurate source localization. In order to improve the accuracy, the results of multiple individual incomplete scan areas can be combined by taking the sum of the error values, see Figure 10(e).

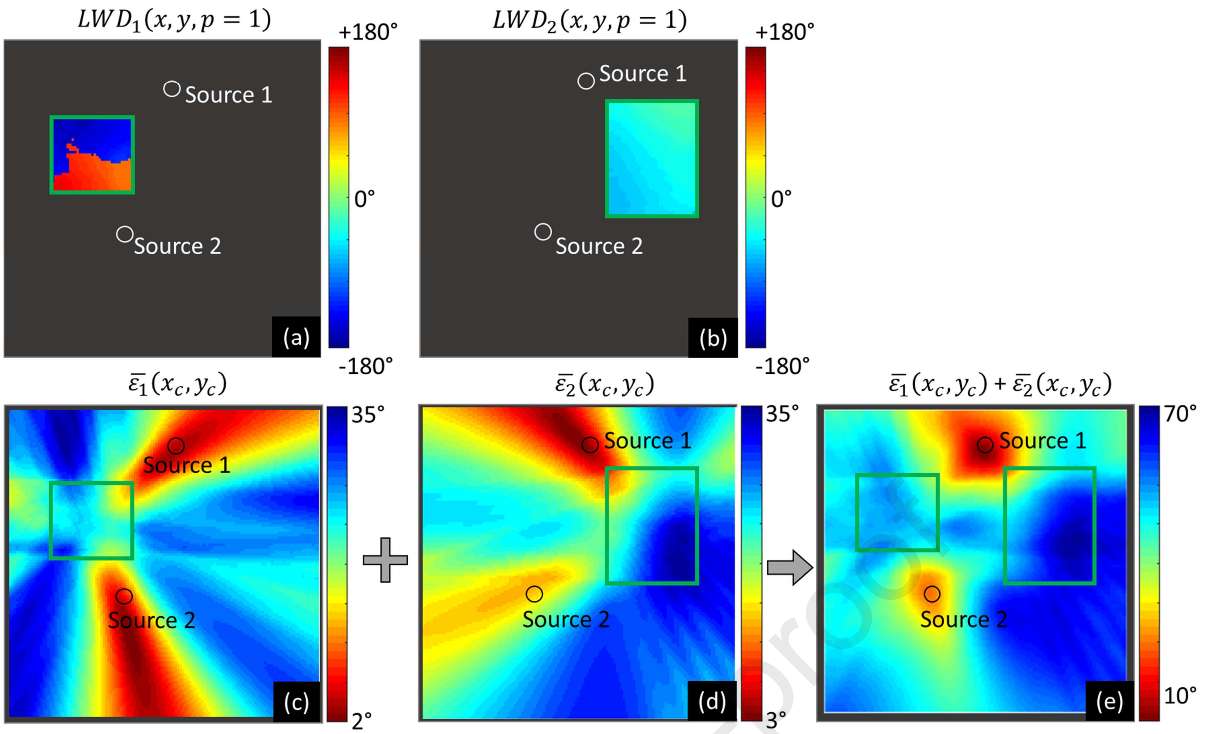

Figure 10: Damage-free CFRP plate with 2 out-of-sight sources: (a-b) Local wave-direction maps for incomplete scan areas (c-d) Local wave-direction error maps for incomplete scan areas (e) Combined error map.

4. Nonlinear local wave-direction estimation for detection of BVID

In the previous section, it was explained how LWDE can be used for localization of sources of propagating waves. From previous studies of the current authors [37, 38], it is known that damages behave as secondary sources of nonlinear vibrational components. As such, a damage detection procedure is proposed where LWDE is used for defect detection by localization of all sources of higher harmonic vibrational components. This nonlinear version of the LWDE is indicated by NL-LWDE. Results are shown for in-sight as well as out-of-sight damage detection.

The same workflow is followed as was schematically illustrated on Figure 2. The only difference is in the first data conditioning step. In previous example, a A_0 mode bandpass filter was used to extract the linear A_0 mode response from the global measurement: $V_z^*(x, y, t) = V_z^{A_0}(x, y, t)$. In this case, the data conditioning handles the extraction of the second order higher harmonic component (HH_2) from the global measurement in combination with a sweep to toneburst conversion: $V_z^*(x, y, t) = V_{z-f_c}^{HH2}(x, y, t)$.

4.1. Data conditioning

The contact acoustic nonlinearity at the defect results in the generation of nonlinear vibrational components. Here, the second higher harmonic component (HH_2) is used as this is the one which typically has the highest amplitude of the higher harmonics [23]. As such, the observed sweep response $V_z(x, y, t)$ needs to be converted to a HH_2 toneburst response $V_{z-f_c}^{HH2}(x, y, t)$. This HH_2 toneburst response is then used as input for the NL-LWDE algorithm. The construction of $V_{z-f_c}^{HH2}(x, y, t)$ requires: (a) the extraction of the HH_2 component and (b) a sweep to toneburst conversion. In this case, it is not necessary to perform an additional A_0 mode bandpass filtering step because the HH_2 component is already dominated by the A_0 mode.

a. Extraction of higher harmonic component

The HH_2 component is extracted from the total sweep response using bandpass filtering in the time-frequency domain. The filtering procedure is explained in detail in a recent publication of the current authors [38]. Here, a short summary is given.

The HH_2 extraction procedure has three steps. First, short-time-Fourier-Transformation (STFT) is used to go from time domain to time-frequency domain. The resulting average spectrogram is shown in Figure 11(a). Straights lines of increased intensity are visible corresponding to the linear sweep response and the higher harmonic components (e.g. HH_2 and HH_3). Secondly, the HH_2 component is extracted from the spectrogram using a bandpass filter in time-frequency domain (see Figure 11(b)). The linear sweep excitation signal had a start and end frequency of 10 and 125 kHz, respectively, so the HH_2 component starts and ends at 20 and 250 kHz, respectively. The resulting filtered spectrogram is shown in Figure 11(c). At last, the HH_2 component is obtained in spatial-time domain after inverse STFT.

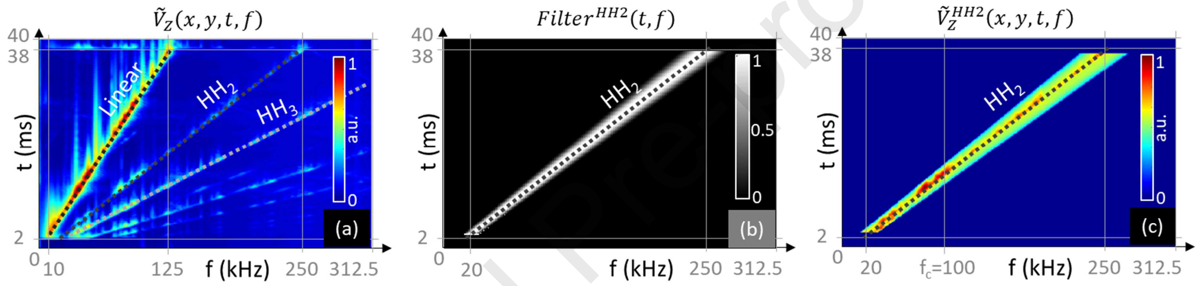

Figure 11: Time-frequency representation (i.e. spectrogram): (a) Total sweep response, (b) HH_2 bandpass filter and (c) Extracted HH_2 component response.

b. Sweep to burst conversion

As the NL-LWDE relies on propagating waves, the HH_2 sweep response $V_z^{HH2}(x,y,t)$ is transformed to a burst response $V_{z-f_c}^{HH2}(x,y,t)$. The transfer function method introduced by Michaels et al. [41] is used to convert the broadband (20 to 250 kHz) HH_2 sweep response to a narrowband 10-cycle Hanning-windowed burst response at center frequency f_c = 100 kHz. This frequency was selected because at 100 kHz a high intensity of the HH_2 component is observed in the spectrogram (see Figure 11(c)). Similar results are obtained for other numbers of cycles.

As a first step, an artificial HH_2 sweep excitation signal $U_{sweep}^{HH2}(t)$ is constructed. This artificial signal is a linear sweep of uniform amplitude with start frequency 20 kHz and end frequency 250 kHz.
Next, the broadband excitation signal $U_{sweep}^{HH2}(t)$, the observed sweep response $V_z^{HH2}(x,y,t)$ and the desired toneburst excitation signal $U_{burst-f_c}(t)$ are converted to the frequency domain using the discrete Fourier transform:

$$\widetilde{U}_{sweep}^{HH2}(f)=\frac{1}{N}\sum_{n=0}^{N-1}U_{sweep}^{HH2}(t)\,e^{-2\pi i\frac{k\,n}{N}}$$
$$\widetilde{V}_{z}^{HH2}(x,y,f)=\frac{1}{N}\sum_{n=0}^{N-1}V_{z}^{HH2}(x,y,t)\,e^{-2\pi i\frac{k\,n}{N}} \tag{10}$$
$$\widetilde{U}_{burst-f_c}(f)=\frac{1}{N}\sum_{n=0}^{N-1}U_{burst-f_c}(t)\,e^{-2\pi i\frac{k\,n}{N}}$$

Next, the ratio of $\widetilde{U}_{burst-f_c}(f)$ over $\widetilde{U}_{sweep}^{HH2}(f)$ is used as a transfer function to obtain the desired burst response:

$$\widetilde{V}_{z-f_c}^{HH2}(x,y,f)=\frac{\widetilde{U}_{burst-f_c}(f)}{\widetilde{U}_{sweep}^{HH2}(f)}\,.\,\widetilde{V}_{z}^{HH2}(x,y,f) \tag{11}$$

At last, the inverse Fourier transformation is performed to obtain the HH_2 burst response in temporal domain (with *n = 0,1,…,N-1*):

$$V_{z-f_c}^{HH2}(x,y,t)=\sum_{k=0}^{N-1}\widetilde{V}_{z-f_c}^{HH2}(x,y,f)\,e^{2\pi i\frac{k\,n}{N}} \tag{12}$$

Figure 12(a) and (b) show time snapshots of the linear as well as the HH_2 burst response. In addition, animations are made available as supplementary material. The linear response was obtained after extracting the linear part using time-frequency filtering (see section 4.1.a.) followed by a burst conversion with f_c = 100/2 kHz = 50 kHz. This signal is not used in the NDT procedure but was constructed solely to make the snapshot in Figure 12(a).

4.2. Nonlinear local wave-direction estimation for in-sight damages

At the moment that the piezoelectric excited wave packet meets the defect (see Figure 12(a)), contact acoustic nonlinearity takes place and the defect acts as a secondary source of the HH_2 component (see Figure 12(b)). Apart from the HH_2 component generated at the defect, there are also HH_2 waves excited by the actuator (sensor nonlinearity). Although these waves are of relatively low amplitude compared to the defect nonlinearity, they affect the NL-LWDE procedure (see further). Note the low amplitude of the HH_2 component which necessitated the use of reflective tape for this SLDV measurement.

In order to construct the observed LWD map, the flowchart shown in Figure 2 and explained in Section 3 is followed. In this case, there are two sources of HH_2 vibrations: the defect and the actuator (see Figure 12(b)). As a result, two peaks are found in the $V_{z-f_c,\,RMS}^{\mathrm{HH2}}(x_3,\mathrm{y}_3,\theta_c)$ curve as shown in Figure 12(c) for the explanatory point $p_3(x_3,y_3)$ marked with a white star. For this particular point, the dominant peak (*p* = 1) corresponds to a propagation direction θ_c = -15° which points to the BVID, whereas the second peak (*p* = 2) is around θ_c = 85° and pointing to the actuator. This observation is reflected in the $LWD(x,y,p)$ maps shown in Figure 13(a,b) for *p* = 1 and *p* = 2, respectively. Note that the explanatory point $p_3(x_3,y_3)$ is again marked with a white star and the dominant wave propagation directions are indicated.

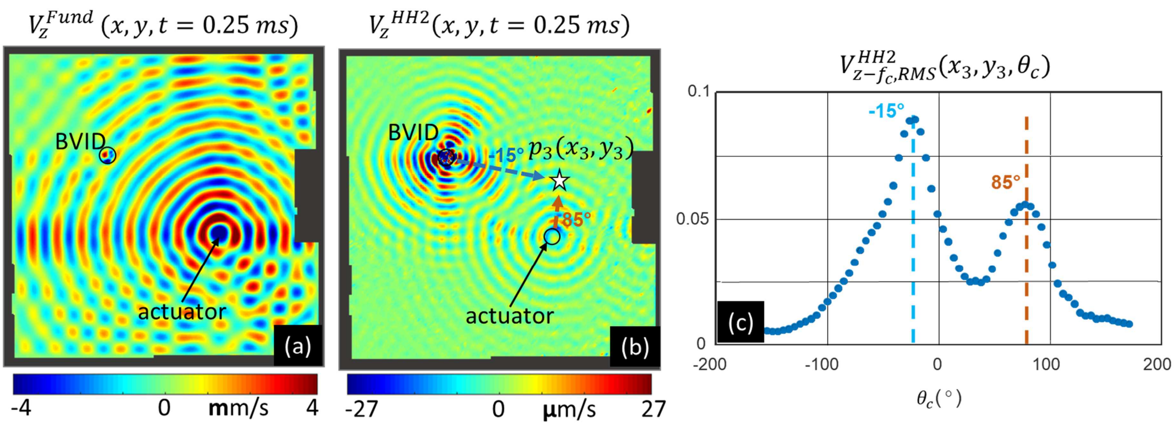

Figure 12: Snapshot in time for the burst response (a) linear component, (b) second higher harmonic component and (c) RMS energy of the HH_2 signal at point $p_3(x_3, y_3)$ in function of the propagation direction θ_c.

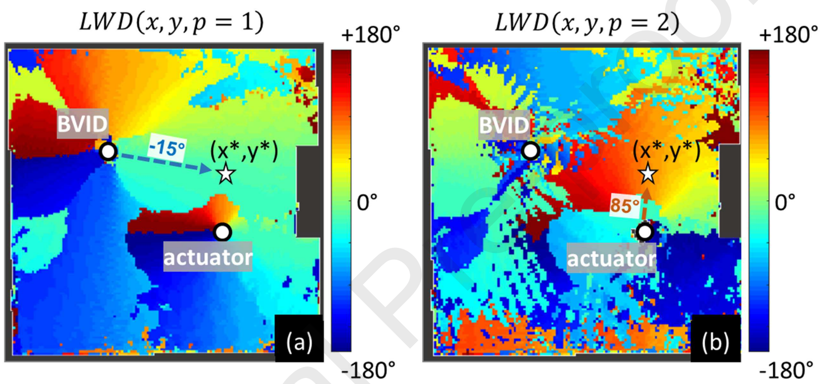

Figure 13: Observed local wave-direction map (a) p = 1, (b) p = 2.

The error map is obtained using Eq. 9 where the virtual LWD^V is constructed assuming a circular wave front (see Eq. 7). Although this material is not quasi-isotropic, the use of the A_0 mode allows to make this assumption. The quasi-circular waveform is also visible in Figure 12(a,b).

For illustration purposes, the error map is first constructed by only looking at the dominant propagation direction at each point (p_{max} = 1). The result is shown in Figure 14(a) and reveals only the dominant source of HH_2 vibrations, which is mainly the BVID. For the error map of Figure 14(b), all detected peaks in the $V_{z-f_c,\ RMS}^{\mathrm{HH2}}(x, y, \theta_c)$ are taken into account (incl. potential edge reflections). It can be seen that by using also the information of the other peaks, both sources of the HH_2 waves are found and the defect is more accurately localized.

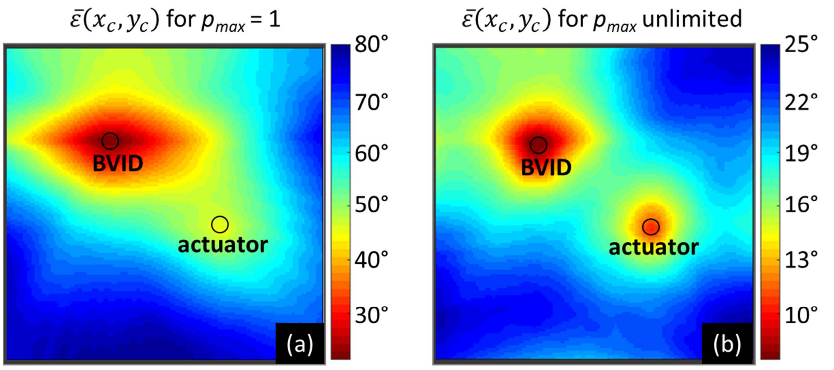

Figure 14: Nonlinear local wave-direction error map for CFRP plate with BVID: (a) Single source assumption (b) Multiple source detection.

4.3. Nonlinear local wave-direction estimation for out-of-sight damages

In the previous section, it was illustrated how NL-LWDE can be used to detect damages without the need of a baseline measurement or user input. While this is certainly promising for NDT in an industrial environment, there are other full-field guided wave NDT approaches which can do the same e.g. local wavenumber estimation [4-8], mode-removed weighted-root-mean-square energy mapping [18, 19, 21] and nonlinear energy mapping [38]. The main advantages of using NL-LWDE for NDT is that the method is promising for detection of very deep defects (see [37, 38]) which might be even out-of-sight.

In order to show the robustness of the NL-LWDE method, four damage maps are constructed where in each case a different incomplete scan area is considered. Moreover, each of these four incomplete scan areas differ in location and shape. The areas are indicated with green rectangles on Figure 15(a-d).

First, the local wave-direction maps are determined and superimposed on Figure 15 (a-d) for p = 1. Next, the error maps $\bar{\varepsilon}(x_c, y_c)$ are constructed using Equation 9. Note again that the coordinates (x_c, y_c) cover the entire component while the points (x, y) are limited to the incomplete scan area. The resulting error maps $\bar{\varepsilon}(x_c, y_c)$ are shown in Figure 15(e-h). For each of these maps, a low error is found at the location of the BVID, even when the incomplete scan area is located relatively close to the sample's edge and close to the excitation position (i.e. cases (d) and (h)). This indicates the robustness of the proposed method.

Very precise localization of the damage is not possible when only a single small incomplete scan area is used. For this it is proposed to use the obtained 'rough' NL-LWDE error map as a fast initial inspection tool. Afterwards, an additional measurement can be performed solely for the areas of increased damage likelihood (i.e. red areas in Figure 15) using a more time-consuming but very accurate NDT method such as the ultrasonic C-scan. Alternatively, multiple distributed small areas can be considered and the obtained error maps can be combined as shown in Figure 15(i,j).

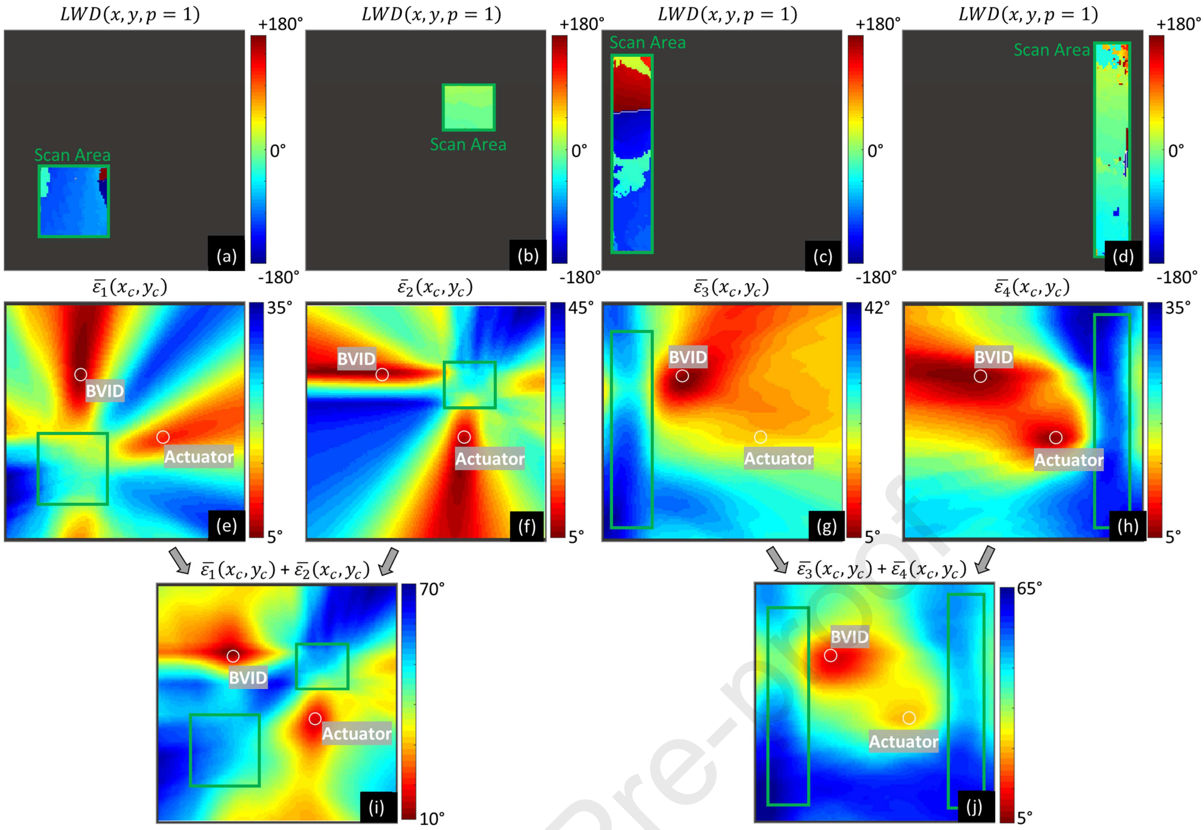

Figure 15: Damage detection using NL-LWDE for 4 cases of an incomplete scan area. (a-d) Local wave-direction maps for p = 1 with indication of the scan area. (e-h) Error maps with indication of the incomplete scan area. (i) Combined error map.

5. Conclusions

Local wave-direction estimation (LWDE) is proposed as a novel method for the localization of propagating wave sources using scanning laser Doppler vibrational measurements. The algorithm makes use of directional bandpass filters in the wavenumber domain in order to determine the dominant wave propagation directions at every scan point. While the location of the sources can already be distinguished in these local wave-direction maps, a global error map is constructed using the virtual local wave-direction field. The resulting error map reveals all the sources as local minima. The proposed algorithm is baseline-free, user-independent and not compromised by possible edge reflections. Considering that the LDWE method exploits wave direction features, it can be used to localize not only in-sight but also out-of-sight sources which may even be correlated.

The LWDE method is introduced for the localization of piezoelectric sources in a quasi-isotropic CFRP plate. This easy to understand example serves as a proof of concept of the method. Every step is explained in detail starting with the easiest case of the detection of a single in-sight source up to the detection of multiple out-of-sight sources.

Next, a nonlinear variant of the LWDE procedure is introduced. NL-LWDE proves successful in localizing the nonlinear response of a barely visible impact damage (as well as the nonlinear response of the piezoelectric actuator) in a cross-ply CFRP plate. Moreover, the out-of-sight damage detection capability is shown, proving the potential of the proposed method for baseline-free detection of potential hidden deep damages in a fast manner.

Acknowledgments

The authors acknowledge Fonds voor Wetenschappelijk Onderzoek FWO (fellowships 1148018N, 1S11520N and 12T5418N) and the SBO project DETECT-IV (Grant no. 160455), which fits in the SIM research program MacroModelMat (M3) coordinated by Siemens (Siemens Digital Industries Software, Belgium) and funded by SIM (Strategic Initiative Materials in Flanders) and VLAIO (Flemish government agency Flanders Innovation & Entrepreneurship).

References

1. Nsengiyumva, W., et al., *Advances, limitations and prospects of nondestructive testing and evaluation of thick composites and sandwich structures: A state-of-the-art review.* Composite Structures, 2021. **256**.
2. Ostachowicz, W., M. Radzieński, and P. Kudela, *50th Anniversary Article: Comparison Studies of Full Wavefield Signal Processing for Crack Detection.* Strain, 2014. **50**(4): p. 275-291.
3. Jurek, M., et al., *Non-contact excitation and focusing of guided waves in CFRP composite plate by air-coupled transducers for application in damage detection.* Procedia Structural Integrity, 2018. **13**: p. 2089-2094.
4. Flynn, E.B., et al., *Structural imaging through local wavenumber estimation of guided waves.* NDT & E International, 2013. **59**: p. 1-10.
5. Rogge, M.D. and C.A. Leckey, *Characterization of impact damage in composite laminates using guided wavefield imaging and local wavenumber domain analysis.* Ultrasonics, 2013. **53**(7): p. 1217-26.
6. Jeon, J.Y., et al., *Damage detection on composite structures with standing wave excitation and wavenumber analysis.* Advanced Composite Materials, 2017. **26**(sup1): p. 53-65.
7. Gao, T., et al., *Hidden Corrosion Detection Using Laser Ultrasonic Guided Waves with Multi-frequency Local Wavenumber Estimation.* Ultrasonics, 2020.
8. Moon, S., et al., *Optimization of excitation frequency and guided wave mode in acoustic wavenumber spectroscopy for shallow wall-thinning defect detection.* Journal of Mechanical Science and Technology, 2018. **32**(11): p. 5213-5221.
9. Glushkov, E., et al., *Wave energy trapping and localization in a plate with a delamination.* Smart Materials and Structures, 2012. **21**(12).
10. Tian, Z., L. Yu, and C. Leckey, *Guided Wave Propagation Study on Laminated Composites by Frequency-Wavenumber Technique*, NASA, Editor. 2014: Langley Research Center.
11. Kudela, P., et al., *Application of scanning laser Doppler vibrometry for delamination detection in composite structures.* Optics and Lasers in Engineering, 2017. **99**: p. 46-57.
12. Munian, R.K., D.R. Mahapatra, and S. Gopalakrishnan, *Lamb wave interaction with composite delamination.* Composite Structures, 2018. **206**: p. 484-498.
13. Glushkov, E.V., et al., *Guided Wave Propagation and Diffraction in Plates with Obstacles: Resonance Transmission and Trapping Mode Effects.* Physics Procedia, 2015. **70**: p. 447-450.
14. Solodov, I., et al., *A local defect resonance to enhance acoustic wave-defect interaction in ultrasonic nondestructive evaluation.* Applied Physics Letters, 2011. **99**(21).
15. Segers, J., et al., *In-plane local defect resonances for efficient vibrothermography of impacted carbon fiber-reinforced polymers (CFRP).* NDT & E International, 2019. **102**: p. 218-225.
16. Segers, J., et al., *Probing the limits of full-field linear Local Defect Resonance identification for deep defect detection.* Ultrasonics, 2020. **105**.
17. Solodov, I. and M. Kreutzbruck, *Single-sided access remote imaging via resonant airborne activation of damage.* NDT & E International, 2019. **107**.

18. Kudela, P., M. Radzienski, and W. Ostachowicz, *Impact induced damage assessment by means of Lamb wave image processing.* Mechanical Systems and Signal Processing, 2018. **102**: p. 23-36.
19. Radzienski, M., et al., *Damage Identification in Various Types of Composite Plates Using Guided Waves Excited by a Piezoelectric Transducer and Measured by a Laser Vibrometer.* Sensors (Basel, Switzerland), 2019. **19**(9).
20. O'Dowd, N.M., et al., *Exploring the Performance Limits of Full-Field Acoustic Wavenumber Spectroscopy Techniques for Damage Detection through Numerical Simulation*, in *8th European Workshop on Structural Health Monitoring*. 2016, NDT.net: Bilbao Spain.
21. Segers, J., et al., *Robust and baseline-free full-field defect detection in complex composite parts through weighted broadband energy mapping of mode-removed guided waves.* Mechanical Systems and Signal Processing, 2020. **Accepted for publication**.
22. Solodov, I., N. Krohn, and G. Busse, *CAN: an example of nonclassical acoustic nonlinearity in solids.* Ultrasonics, 2002. **40**(1): p. 621–625.
23. Jhang, K.-Y., et al., *Measurement of Nonlinear Ultrasonic Characteristics*. Measurement Science and Technology, ed. M.G. Cain, et al. 2020: Springer.
24. Van Den Abeele, K., et al., *Nonlinear Elastic Wave Spectroscopy (NEWS) Techniques to Discern Material Damage, Part II: Single-Mode Nonlinear Resonance Acoustic Spectroscopy.* Res Nondestr Eval 2000. **12**: p. 31–42.
25. Zhang, S., et al., *Far-sided defect recognition of FRP sandwich structures based on local defect resonance.* Journal of Sandwich Structures & Materials, 2019: p. 1-12.
26. Fierro, G.P.M. and M. Meo, *Nonlinear elastic imaging of barely visible impact damage in composite structures using a constructive nonlinear array sweep technique.* Ultrasonics, 2018. **90**: p. 125-143.
27. Fierro, G.P.M. and M. Meo, *A combined linear and nonlinear ultrasound time-domain approach for impact damage detection in composite structures using a constructive nonlinear array technique.* Ultrasonics, 2018. **93**: p. 43-62.
28. Ginzburg, D., *Damage Propagation and Detection using Nonlinear Elastic Wave Spectroscopy in Aerospace Structures*, in *Department of Mechanical Engineering*. 2016, University of Bath.
29. Ooijevaar, T.H., et al., *Nonlinear dynamic behavior of an impact damaged composite skin–stiffener structure.* Journal of Sound and Vibration, 2015. **353**: p. 243-258.
30. Broda, D., et al., *Modelling of nonlinear crack–wave interactions for damage detection based on ultrasound—A review.* Journal of Sound and Vibration, 2014. **333**(4): p. 1097-1118.
31. Van Den Abeele, K., P.A. Johnson, and A. Sutin, *Nonlinear Elastic Wave Spectroscopy (NEWS) Techniques to Discern Material Damage, Part I: Nonlinear Wave Modulation Spectroscopy (NWMS).* Res Nondestr Eval 2000. **12**: p. 17–30.
32. Pieczonka, L., et al., *Damage imaging in composites using nonlinear vibro-acoustic wave modulations.* Structural Control and Health Monitoring, 2017.
33. Dziedziech, K., et al., *Efficient swept sine chirp excitation in the non-linear vibro-acoustic wave modulation technique used for damage detection.* Structural Health Monitoring, 2017. **17**(3): p. 565-576.
34. Klepka, A., et al., *Impact damage detection in composite chiral sandwich panels using nonlinear vibro-acoustic modulations.* Smart Materials and Structures, 2013. **22**(8).
35. Dionysopoulos, D., et al., *Imaging of barely visible impact damage on a composite panel using nonlinear wave modulation thermography.* NDT & E International, 2018. **95**: p. 9-16.
36. Kober, J. and Z. Prevorovsky, *Theoretical investigation of nonlinear ultrasonic wave modulation spectroscopy at crack interface.* NDT and E International, 2014. **61**: p. 10-15.
37. Segers, J., et al., *Backside delamination detection in composites through local defect resonance induced nonlinear source behaviour.* Journal of Sound and Vibration, 2020. **479**.
38. Segers, J., et al., *Nonlinear Elastic Wave Energy Imaging for the Detection and Localization of In-Sight and Out-of-Sight Defects in Composites.* Applied Sciences, 2020. **10**(3924).

39. Spronk, S.W.F., et al., *Comparing damage from low-velocity impact and quasi-static indentation in automotive carbon/epoxy and glass/polyamide-6 laminates.* Polymer Testing, 2018. **65**: p. 231-241.
40. Michaels, T.E., J.E. Michaels, and M. Ruzzene, *Frequency-wavenumber domain analysis of guided wavefields.* Ultrasonics, 2011. **51**(4): p. 452-66.
41. Michaels, J.E., et al., *Chirp excitation of ultrasonic guided waves.* Ultrasonics, 2013. **53**(1): p. 265-70.

Highlights

- Local wave-direction estimation (LWDE) is proposed for source localization.
- In-sight and out-of-sight sources are found using LWDE.
- LWDE is applied in the nonlinear regime (NL-LWDE) and used for defect detection in a CFRP component.
- NL-LWDE is used successful for detection of out-of-sight BVID in an automated and baseline-free manner.

Declaration of interests

☒ The authors declare that they have no known competing financial interests or personal relationships that could have appeared to influence the work reported in this paper.

☐The authors declare the following financial interests/personal relationships which may be considered as potential competing interests: